PneuPrint: 3D printing on inflatables

Che Wei Lin[1] · Gabriele Mattei[2] · Ina Cheibas[3] · Chaoyu Du[2] · Petrus Aejmelaeus-Lindström[3] · Fabio Gramazio[3]

Abstract

This research investigated the feasibility of thermoplastic 3D printing on inflatable membranes. Five experiments were performed in an iterative process through design and manufacture (1), computational simulation and 3D scanning (2), and robotic fabrication on the pneumatic formwork (3). These experiments ranged from small to large-scale 3D printing. Experiment 1 demonstrated the small-scale feasibility of the process and the need to integrate an air-pressure control loop. Experiment 2 investigated the technique transfer from small to large-scale. Experiment 3 analyzed the deviation and shape accuracy of the inflatable membrane. Experiment 4 identified the required fabrication settings and compatibility between the membrane and the 3D printing material. Finally, Experiment 5 demonstrated the design and fabrication potential of large-scale 3D printed elements on pneumatic formworks. The results proved high potential for building freeform design elements for architectural applications on pneumatic formworks.

Keywords Freeform architecture · Digital fabrication · Non-planar 3D printing · 3D scanning · Pneumatic formwork

Introduction

Freeform design, also known as double curved or curvilinear, is one of the most emblematic building expressions in architecture. Freeform features a non-rectilinear configuration of architectural structures where two curves are placed in two different directions, creating a complex and organic form [1, 2]. World-renowned architects have used freeform expressions to create cultural landmarks and iconic buildings, such as the Guggenheim Museum Bilbao, the Sydney Opera House, and the Heydar Aliyev Center [3–5]. This expression allows architects to experiment with novel forms and materials, which can lead to new discoveries and breakthroughs that influence the direction of the architecture discipline as a whole [6]. Furthermore, freeform structures can be functionally advantageous because they distribute forces evenly throughout the building element, which can improve its strength and stability [7]. Funicular shapes, which are structural-informed freeform designs, can distribute stress attained by self-weight in pure compression condition without bending, in contrast to straight or flat structures. These shapes are structurally efficient and environmentally friendly because their form follows the force flows in the geometry, reducing the quantity of materials needed, eliminating the need for additional reinforcement, and allowing for the use of more affordable materials with lower strength [8].

In the past decade, advances in technology such as digital fabrication, and parametric design have further enabled the potential of freeform architecture [9–11]. These tools have allowed architects to explore new forms and shapes that were previously impossible to achieve [12, 13]. To build these shapes, several fabrication techniques can be used, such as subtractive, net-shape (reshape and molds), or additive [14, 15]. 3D printing, also known as additive manufacturing (AM), is the most commonly used method today for producing

✉ Ina Cheibas
cheibas@arch.ethz.ch

Che Wei Lin
lin@arch.ethz.ch

Gabriele Mattei
mattei@arch.ethz.ch

Chaoyu Du
chaoyu.du@arch.ethz.ch

[1] Department of Architecture, Digital Building Technologies, ETH Zürich, Zurich, Switzerland

[2] Department of Architecture, Block Research Group, ETH Zürich, Zurich, Switzerland

[3] Department of Architecture, Chair of Architecture and Digital Fabrication, ETH Zürich, Zurich, Switzerland

freeform designs. This is because 3D printing has the ability to quickly produce complex and unique geometries with high accuracy and precision [16, 17]. Compared to other digital fabrication techniques, 3D printing enables architects to fabricate a physical model directly from a digital model, which allows for greater design flexibility and iteration [18]. This is particularly useful for freeform designs that often involve irregular, organic shapes, difficult or impossible to create with conventional manufacturing techniques. Additionally, 3D printing can reduce material waste and lower production costs compared to other fabrication methods, because this process optimizes material deposition in the required location [19–21].

Material extrusion, also known as Fused Deposition Modeling (FDM), is the prevalent 3D printing method used in architecture for large-scale projects. Material extrusion is a layer-by-layer deposition technique where the extruded material is fed in a continuous stream through a generally heated nozzle [22]. This technology became popularized because it can produce structures using a wide variety of materials, including thermoplastic, concrete, clay, and metal. Thermoplastic is a 3D printing material highly beneficial for translucent, nearly transparent components at an architectural scale [23]. Concrete has been widely used for structural elements, often in combination with added reinforcements [24, 25]. Clay-based materials have the advantage of low environmental impact [26], while metal has been mostly used for high precision nodes and some large-scale elements [27–29]. All these materials can be generally 3D printed in uniform planar or non-planar slicing (Fig. 1a) [30]. Non-planar is considered more advantageous for freeform architecture due to higher geometrical versatility, improved quality, and diminished material waste [31].

Both planar and non-planar slicing methods encounter challenges prominently in large-scale fabrication [32]. Geometry deformation often occurs and limits the design space because of overhang at lower angles below 45° [33], see Fig. 1b. To solve this issue, small-scale 3D printing generally uses additional support materials [34, 35]. In large-scale fabrication, molds or support materials, such as gel or foam, have been used as support to prevent the risk of adhesion between the 3D print and the support structure [36, 37]. Compared to support materials, adaptive molds have gained increased interest for architects and manufacturers

in the past decade. These support structures can be rigid or flexible and offer advantageous solutions due to their reliability and scalability. For example, North Sails, a yacht sail manufacturer, used pneumatic rigid supports structures to produce custom sails and reduce costs by re-using the same reconfigurable mold [38]. A similar adaptive mold has been used by Raun et al. to build architectural glass fiber reinforced concrete (GFRC) panels in an automated process [39]. Furthermore, Christopher et al. explored sub-additive 3D printing, which enabled concrete 3D deposition on a rigid structure that can be mechanically shaped [40]. Nevertheless, rigid formworks are costly systems, can produce waste, have limited degrees of freedom, and can be difficult to maintain, and repair [41, 42]. In contrast, flexible or fabric formwork are more cost effective, reliable, efficient in installation, and have low maintenance [43]. For example, Isler`s hanging models of flexible formwork have been employed in the past to generate inverted shape of funicular shells [44]. More recent examples can be found in fabric-formed structural elements, produced through different tensioning of the membrane [45]. Other researchers investigated the potential to fabricate on textiles as formwork [46–48].

However, flexible formwork can be challenging to use as a support structure due to its tendency to sag or bulge naturally from loading conditions. For this reason, securing high accuracy of the pneumatic shape can be a great impediment as large-scale 3D printing supports. Furthermore, to achieve high accuracy, real-time sensor-based feedback is essential for manufacturing the freeform surface efficiently. To solve these issues, pre-stressing or air support can offer shape stability and enable the potential of flexible membranes as formwork. Such an approach has been already proven for small-scale 3D printed auxetic lattices [49]. Additionally, Stuttgart University combined pneumatic formwork and robotic fiber weaving as the fabrication method [50]. This "Water spider" pavilion has demonstrated how to transform an air-supported structure into a self-supporting shell with a sensor-based feedback loop. Thus, air-supported membrane, or pneumatic formwork, has a great potential for freeform 3D printed elements.

Therefore, this study aims to identify the feasibility of 3D printing on a pneumatic formwork for complex freeform designs. Material extrusion of thermoplastic with non-planar slicing method has been selected as the large-scale

Fig. 1 **a**) Example of uniform planar slicing (left geometry) and non-planar slicing (right geometry); **b**) Geometry deformation in a thermoplastic 3D printed design, because of overhang failure in angles below 45°
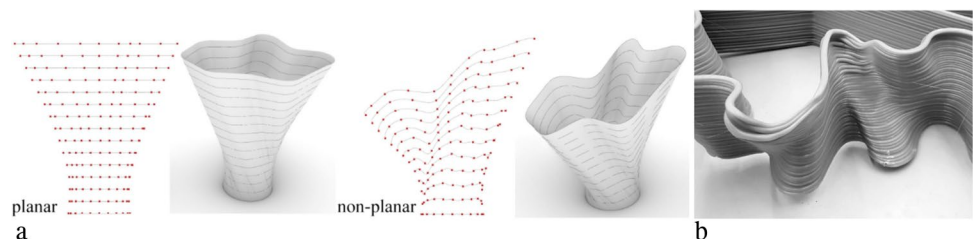
fabrication technique. Furthermore, to identify geometry accuracy, a sensor-based feedback loop of scanning and simulating the pneumatic formwork has been used. Five experiments were tested to identify the best strategy for an accurate outcome.

Method

In this section, the study methodology is presented. The experiments were performed in an iterative process divided into three steps: (1) pneumatic formwork system, (2) digital process, and (3) fabrication, as shown in Fig. 2. First, a pneumatic form (1) was built, where strategies were identified in terms of dimensions, membrane material, and boundary conditions. Second, digital tools (2) were used to simulate the shape of the pneumatic formwork using the dynamic relaxation method [51]. The simulation model accuracy was then verified by scanning the physical formwork. Third, 3D print toolpaths were generated for the fabrication process (3) based on the scanning results. With this

experimental method and setup, five 3D-printed prototypes were manufactured.

Pneumatic formwork system

The strategy for building the pneumatic formwork considers three key aspects: i) formwork assembly, ii) pressure control of inflating the pneumatic formwork, and iii) membrane type.

The pneumatic formwork (i) is assembled as a three-layered structure—a baseboard, an elastic membrane, and a frame, see Fig. 3a. The membrane is clamped between the baseboard and the frame to create an airtight chamber. The material for the baseboard and the frame are made of plywood. The baseboard is sealed with silicon and covered with polyvinyl chloride (PVC) film layer to prevent air and pressure loss. A neoprene gasket can be embedded in the baseboard and the frame to minimize any possible air leaks at the contact between the plywood and the membrane surface. Additionally, magnets can be added in the middle of the membrane to modify the shape of the surface.

Fig. 2 Diagram of the methodology. The experiments consist of an iterative process divided into three main steps: (1) pneumatic formwork, (2) digital process, and (3) fabrication
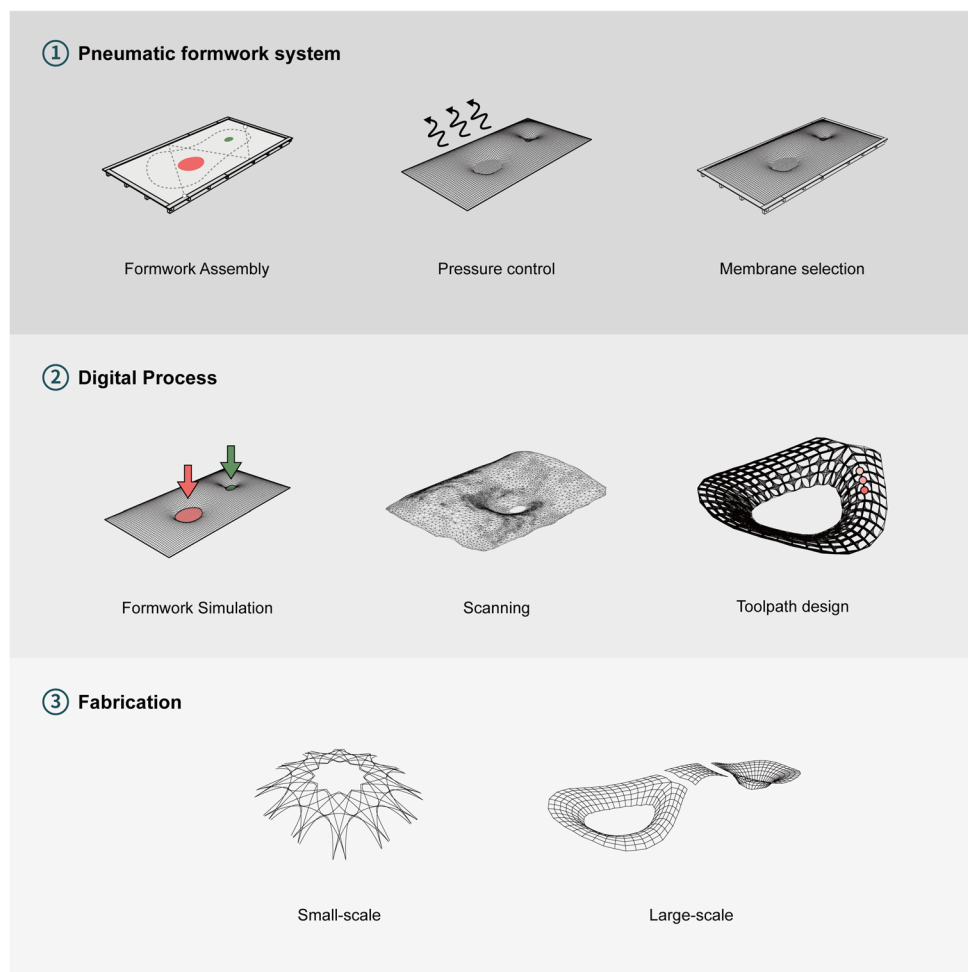
Fig. 3 **a**) Assembly of the pneumatic formwork in a three-layered configuration: a frame (A), a membrane (B), a baseboard (C), and neoprene gaskets (D); **b**) Pneumatic system loop for air-pressure control: solenoid valve (A), pressure regulator (B), pneumatic formwork (C), BME280 pressure sensor (D), and Arduino UNO (E)
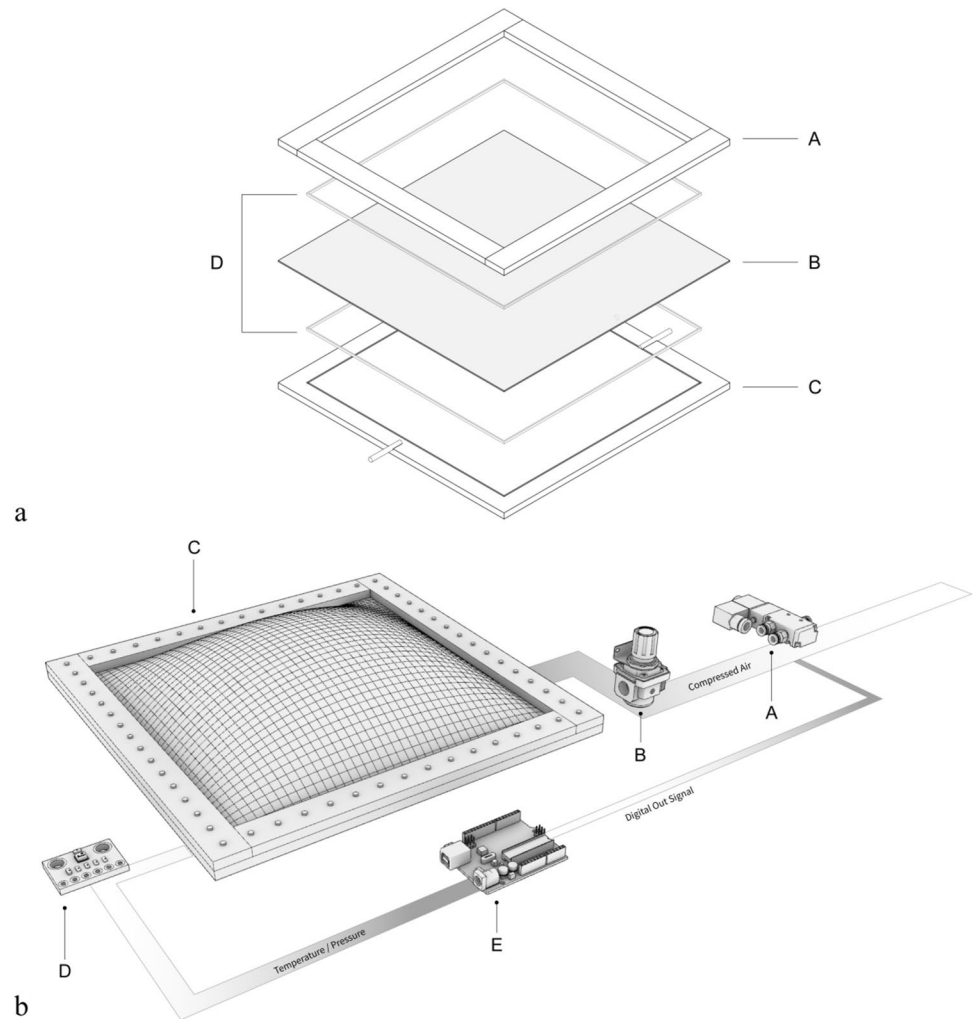
Figure 3b displays a customized pressure control loop (ii) built to maintain consistent inner pressure in the inflated membrane. The system consists of an Arduino UNO, a BME280 pressure sensor, a solenoid valve, and a pressure regulator. The Arduino activates or deactivates the solenoid valve based on the low-pass filtered pressure. The valve and the manual pressure regulator control the inlet air pressure. The regulator helps to prevent pressure deflection caused by the sensor latency.

The membrane material (iii) is selected based on the compatibility between the elasticity of the membrane and the 3DP material service temperature, see Fig. 4. 3D printing temperatures have relatively high values, between 190 and 250 °C that can melt the membrane if the service temperature of the inflatable is too low. In this study, three membranes were selected due to their advantageous material properties, such as high service temperature, high elasticity, and large available dimensions within ready market availability. The materials for the membrane are latex from a weather balloon, 50 shore-A 0.5 mm thick silicone, and 35

shore-A 1 mm thick silicone [52, 53]. The 35 shore-A1 mm thick silicone membrane was found as the material with the most advantageous properties, with a continuous service temperature of 200 °C and a peak temperature of 230 °C. Its tensile strength is 14 MPa and elongation at break is 880%.

These material properties are essential in the dynamic relaxation method to precisely simulate the pneumatic geometry. The silicone membrane is generally used in the vacuum press industry for manufacturing processes for Cross Laminated Timber [54]. Thus, architectural-scale dimensions are market readily available.

Digital process

The digital process uses several computational tools and consists of three steps:

1. Simulation of the inflatable using a dynamic relaxation method,

Fig. 4 Compatibility between the membrane and 3D printing thermoplastics service temperature
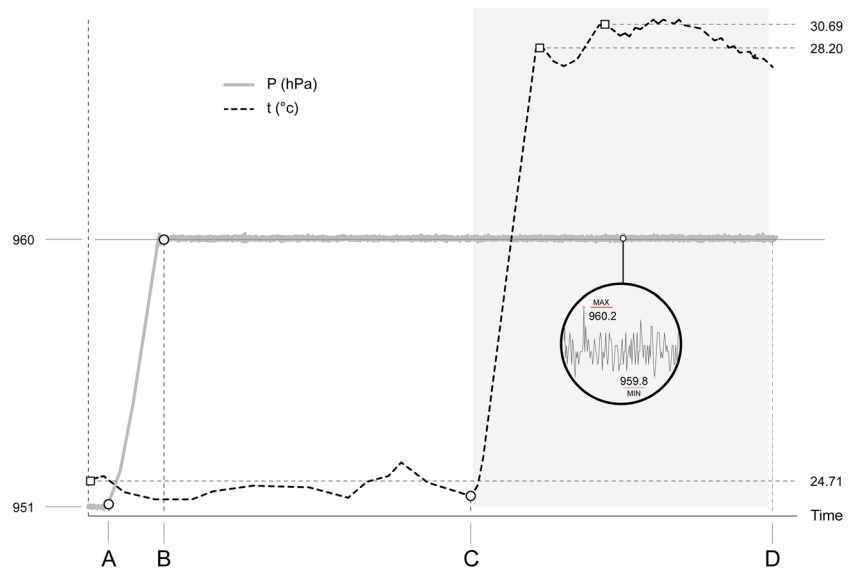
2. 3D scanning of the inflatable and comparative analyses with the simulated input,
3. Design of the 3D printing toolpath on the 3D scanned result.

The simulation is required to design the inflatable membrane, while 3D scanning is needed to determine if the physical prototype matches that simulation while obtaining a precise representation of the formwork.

Simulation process

The dynamic relaxation method implemented in a COMPAS framework was employed to design and simulate the inflatable behavior [51, 55]. First, a mesh representing the not-inflated membrane was created in Rhino Grasshopper [56]. This mesh was designed from the constraints where specific vertices were identified as anchors, as shown in Fig. 5a. Then, the mesh was exported as a JSON file and

Fig. 5 a) Constraints possibilities for the pneumatic membrane. From left to right: i) placement of magnets, ii) placement of cables, iii) additional frame placement; **b)** Geometry and residual forces (A) results from the dynamic relaxation method
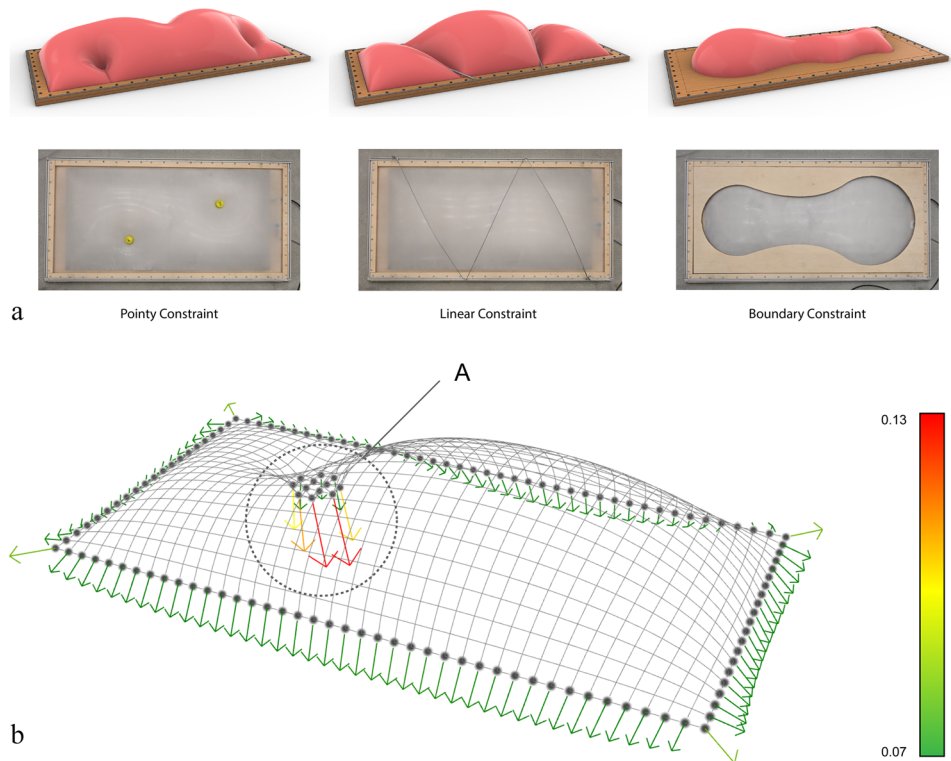
used as input for the dynamic relaxation algorithm in the COMPAS framework. Once the E-modulus of the membrane (GPa), and internal pressure (hPa) were generated, the algorithm was able to calculate the form in equilibrium as well as its residual forces, see Fig. 5b. In particular, for experiment 5, the calculated residual forces were used to estimate the weight of the constraining magnets placed on the membrane (detailed further in section *Experiment 5—Chapter 3*). Finally, the mesh was imported as JSON file for toolpath planning and visualization in Rhino Grasshopper.

Scanning

The pneumatic membrane has no bending stiffness, which can generate deformations due to the internal pressure, material imperfections, and environmental disturbance. For this reason, 3D scanning was used to identify the exact membrane shape and accurate location for the 3D printing

process. An Intel Realsense D415 stereo depth camera was placed at the robotic arm's end-effector and was able to perform scanning from multiple angles and distances, see Fig. 6a [57]. A Visual fiducial markers, such as the AprilTag, were attached to the corners of the formwork frame, see Fig. 6a [58]. These markers helped identify the formwork boundary and filter background noise in the scanning data. Moreover, a distance threshold was applied to remove additional noise.

In the scanning process, the end-effector was moved to a location with maximum visibility of the AprilTag. Then, the location of the tool center point (TCP) and the tags were recorded, the scan was performed, and the process was repeated until the formwork was scanned from multiple various angles.

The scanned data was processed via Open3D in python [59]. The point clouds were transformed using the paired TCP frame and aligned using an iterative closest point (ICP)
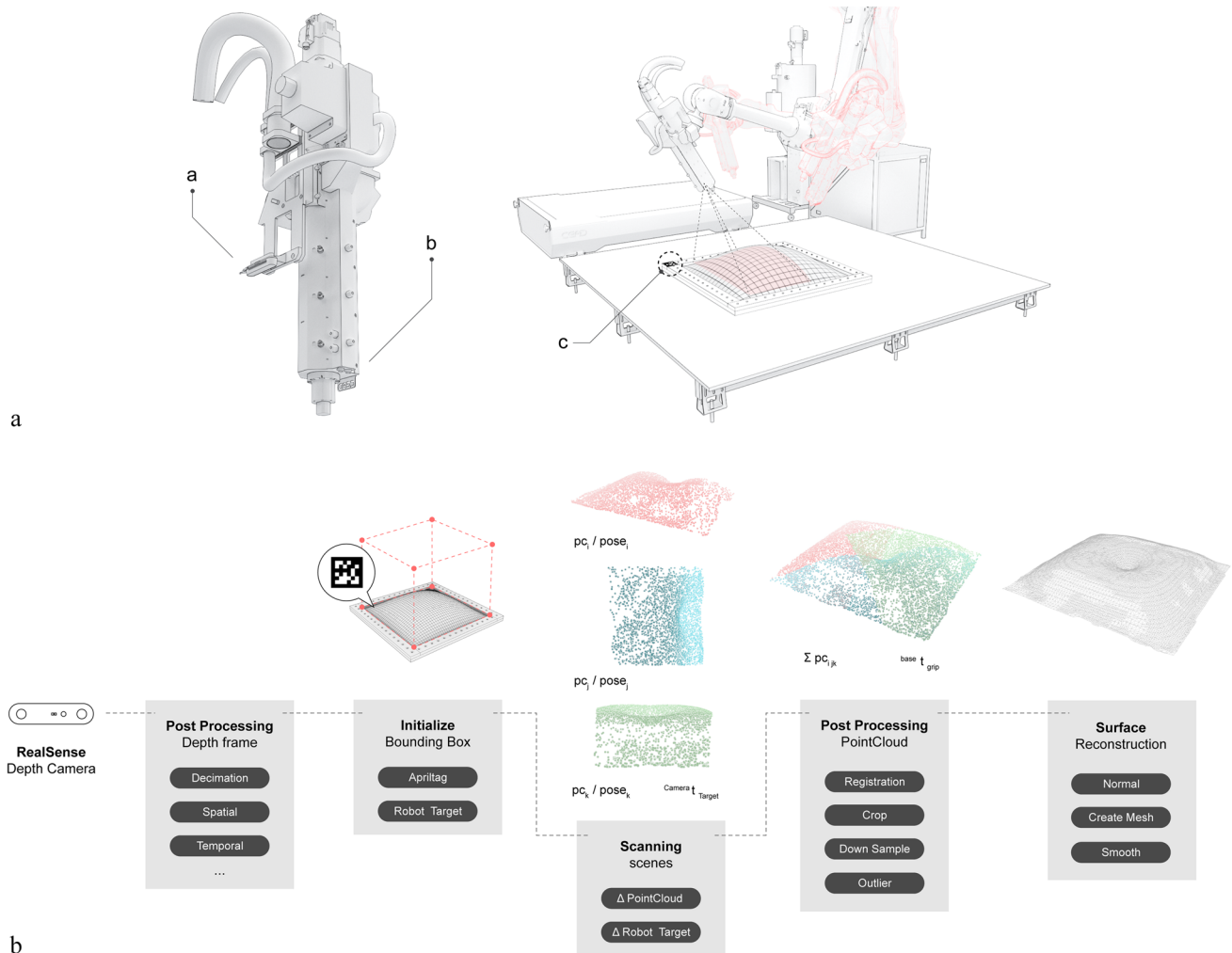

Fig. 6 a) 3D scanning set-up of the Realsense camera (a) placed at the robotic arm end-effector (b) and Apriltag (c) placed on the pneumatic formwork; **b**) 3D scanning process flow chart

algorithm [60]. The aligned point clouds were downsampled to reduce computation time. Subsequently, a statistical point cloud outlier algorithm was performed to remove contained noise and artefacts before surface reconstruction. A Poisson surface reconstruction method was used to create a smooth mesh surface out of the combined point clouds [61]. Figure 6b displays all these steps in the scanning process.

Toolpath planning

The toolpath planning was designed in Rhino/Grasshopper [56]. The design was based on the point coordinates extracted from the mesh in the scanning process. Then, these points and their surface normal on the mesh were converted into TCP in COMPAS RRC for point-to-point robotic control [62]. Collision avoidance and detection were also analyzed between the extruder and the membrane. The collision occurs when the print areas are closer to the internal constraints, and the membrane has a quasi-horizontal surface normal, see Fig. 7a. Therefore, before fabrication, the scanned pneumatic formwork and surroundings were imported in a RobotStudio™ virtual scene [63]. This simulation contributed to create a visual representation for detecting robotic collision. The robotic joint axis angle

were analyzed during this simulation to avoid singularity or axis coupling and ensure print quality in the fabrication process. Figure 7b displays how the opposite angles for joint axis-4 and joint axis-6 caused an unexpected acceleration or deceleration. The TCP frames were modified accordingly based on the angle visualization to avoid bad print quality. Specifically, the extruder nozzle was secured from reaching inaccessible parts of the membrane by applying TCP normal optimization. The TCP normals were limited in the range of 30° angle of the Z-axis robot world coordination system while simultaneously matching to the perpendicular direction of the pneumatic surface. Once the normal was fixed, TCP reorientation was applied to maximize robot reachability and solve significant deceleration.

Fabrication setup

This research uses two robotic fabrication setups with a UR-10 robotic arm and an ABB IRB-4600 robotic arm. The UR-10 robotic arm is used for initial tests in a small-scale fabrication setup, see Fig. 8a [64]. Attached to its end effector is an E3D SuperVolcano filament extruder [65]. In this process, a 2.85 mm polylactic acid (PLA) filament is used as 3D printing material. PLA is selected due to its vast market

Fig. 7 a) Normal optimization of the TCP frame. The constraint area (b) determines the extruder angle (a) to avoid collision; **b**) Angle data of each join, J4, J5, and J6, of the ABB robot during the printing process
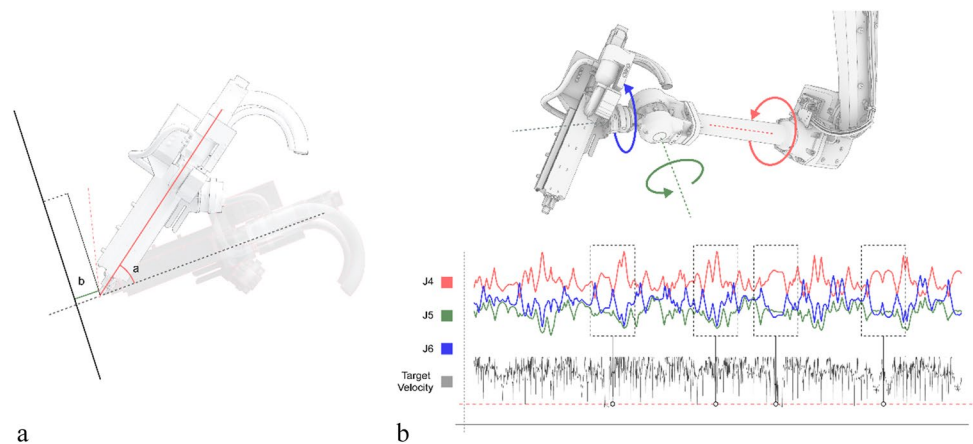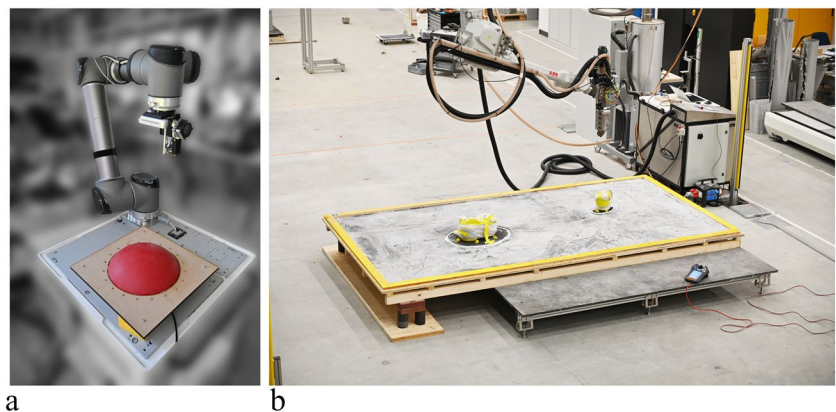
a

b

Fig. 8 a) Small-scale fabrication setup with an UR10 robotic arm, SuperVolcano extruder, and Intel RealSense camera attached to the end-effector; **b**) Large-scale fabrication setup in the Robotic Fabrication Laboratory (RFL) with ABB IRB-4600 robotic arm and CEAD extruder

a

b

availability in the 3D printing field [66]. Figure 8b displays the large-scale fabrication setup installed in the Robotic Fabrication Laboratory (RFL) at ETH Hönggerberg [67]. An ABB IRB-4600 robotic arm has a CEAD thermoplastic extruder placed as an end-effector [68, 69]. The ABB IRB-4600 robotic arm is mounted on a three-axis gantry system, has six degrees of freedom, and has a working area of $3 \times 1.5 \times 3$ m. The CEAD pellet extruder has a maximum material output of 12 kg/h and can extrude a wide range of thermoplastic pellets. It incorporates a complete package that includes a printing bed, nozzle variety from 2 to 12 mm in diameter, material drying, material feeding, and automatic logging of parameters. The 3D thermoplastic materials used in manufacturing the prototypes are PETG and PLA pellets. The experiments conducted on the large-scale setup have the following main fabrication parameters: 2–3 mm layer height, 2 mm layer width, and 60 mm/s printing speed.

Experiments and results

In this section, five experiments are presented, with results displayed at the end of each subchapter. The first prototype is 3D printed with the small-scale UR10 robotic arm, while the following four prototypes, Prototype 2, 3, 4, and 5, are fabricated with the large-scale ABB robotic arm. All prototype fabrication settings are displayed in Table 1.

Experiment 1

The first experiment aimed to identify the 3D printing feasibility on a pneumatic formwork. It uses a small-scale robotic fabrication setup to identify the method's feasibility, from simulation to scanning and fabrication.

In this first experiment, a pneumatic formwork with the size of 300×300 mm was built, see Fig. 9. The formwork comprised three layers: a square medium-density fibreboard (MDF) plate as a baseboard with the air inlet underneath, a latex elastic membrane, and a second cut MDF frame clamped on the top with metallic screws. The elastic membrane was selected due to its ability to achieve reconfigurable shapes by modifying the boundary constraints. However, the air pressure was operated manually, where constant compressed air of 2 kg/cm2 inlet was required to maintain the inflated geometry. The Realsense camera was attached to the end-effector of the UR10 robotic arm and 3D scanned the pneumatic formwork. However, the scanning process was inaccurate due to the significant deviation in the pressure

Table 1 Fabrication settings for the five 3D printed prototypes

No.	Parameters	Prototype 1	Prototype 2	Prototype 3	Prototype 4	Prototype 5
1	Fabrication set-up	UR-10	ABB-IRB 4600	ABB-IRB 4600	ABB-IRB 4600	ABB-IRB 4600
2	Material	PLA	PLA	PLA	PETG	PETG
3	Environment temperature	24.2° C	26.0° C	24.5° C	22.7° C	21.5° C
4	Layers	2	4	6	1	20
5	Average print path length per layer	5.24 m	16.92 m	19.51 m	31.23 m	75.32 m
6	Layer height	1 mm	2 mm	3 mm	3 mm	*3 mm
7	Layer width	2 ± 0.4 mm	4.1 ± 0.3 mm	3.8 ± 0.4 mm	3.8 ± 0.3 mm	*3.8 ± 0.5 mm
8	Nozzle diameter	2 mm	4 mm	4 mm	4 mm	4 mm
9	Extruder temperatures	210° C	190, 195, 205, 210° C	190, 195, 205, 210° C	225, 230, 240, 245° C	225, 230, 240, 245° C
10	Robot speed	10 mm/s	30 mm/s	50 mm/s	60 mm/s	60 mm/s
11	Weight	10 g	714 g	870 g	238 g	33.3 kg
12	Fabrication time	35 min	0 h 37 min	0 h 32 min	0 h 9 min	14 h 51 min

*For Prototype 5, different layer heights were used to accommodate the non-planar design (detailed in Fig. 17c). In consideration to a constant extrusion rate, the corresponding print line widths are averaged

Fig. 9 Small-scale sample printed with transparent PLA filament on MDF formwork
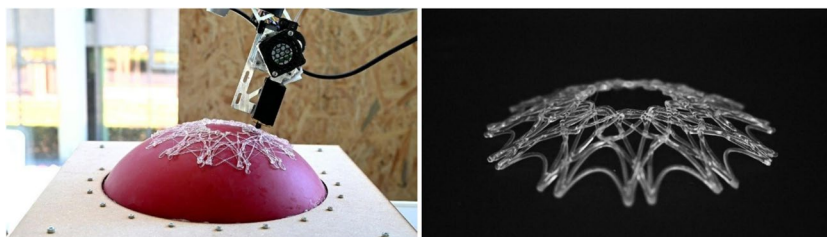
control. In this experiment, no simulations were made. The toolpath was designed as a 2D geometry, and then projected on the 3D scanned mesh. The toolpath was then generated in Grasshopper and used to fabricate Prototype 1 from transparent PLA filament at 210 °C temperature.

Experiment 1 showed a successful robotic fabrication on pneumatic formwork. The latex membrane did not melt due to the nozzle printing temperature. However, the shape of the pneumatic membrane was challenging to control. The slightest pressure instability notably deforms the inflated geometry, thus further affecting the 3D printing process accuracy. This experiment displayed that a control loop for air permeability is required in this process.

Experiment 2

Experiment 2 was the first test on a large-scale robotic fabrication setup. This test aimed to verify the feasibility of transfer from model to architecture-scale manufacturing. The pneumatic formwork was built on a baseboard of 1000×1000 mm. The formwork layers are made of a plywood base, a neoprene gasket, a membrane, and a wooden frame surrounding it, see Fig. 10a. The membrane material was a 50 shore-A 0.5 mm thick silicone, more suitable for higher 3D printing temperatures than latex, with an elongation of 370% and tensile strength of 8 mPa. A pressure control loop was built for Prototype 2 to achieve maximum accuracy of the inflated shape, as described in Sect. "Pneumatic formwork system", see Fig. 10b. The pressure and temperature data were analyzed and documented in real-time during manufacturing, see Fig. 10c.

The simulation of the inflatable was generated with the dynamic relaxation method, as described in Sect. "Simulation process". The scanning process compared the simulated geometry to the physical pneumatic formwork. A statistical outlier removal algorithm was performed to remove noise. In addition, a mesh representing the membrane was created by the Poisson surface reconstruction algorithm. This method resulted in a smoothened mesh surface, which is ideal for toolpath projection. In this computational step, as a first fabrication test, a simple grid geometry was designed and projected on the mesh, see Fig. 10d. The grid dimensions were 700 mm × 700 mm and 6-layer height of 2 mm per layer. PLA pellets were used to fabricate Prototype 2 as 3D printing thermoplastic material due to their lower melting temperature (210 °C) compared to other thermoplastic materials, see Fig. 10e.

Experiment 2 displayed that architectural-scale 3D printing on pneumatic formwork is possible. In this experiment, it has been proven that a pressure control loop was essential to achieve an stable position of the membrane and further generate the toolpath design. Nevertheless, the main challenge of the experiment was air permeability. For this

reason, Experiment 2, compared to Experiment 1, had an additional neoprene gasket applied around the wooden frame to eliminate the air leakage. As a result, this gasket reduced the pressure descent to 1 hectopascal/second (hPa/sec). However, this value was still insufficient for maintaining a steady pneumatic formwork for 3DP fabrication. Therefore, the pressure control loop was a key step in the large-scale fabrication setup. The difference between the formwork and the atmospheric pressure refined the target pressure. Within the range of 2 hPa and 10 hPa, the target pressure remained stable within a tolerance of 0.2 hPa, see Fig. 11. Data from the sensor illustrates the accuracy of the pressure control loop, where the formwork deformation caused by the 0.2 hPa pressure ripple is within the nominal margin of a 2 mm or higher print height.
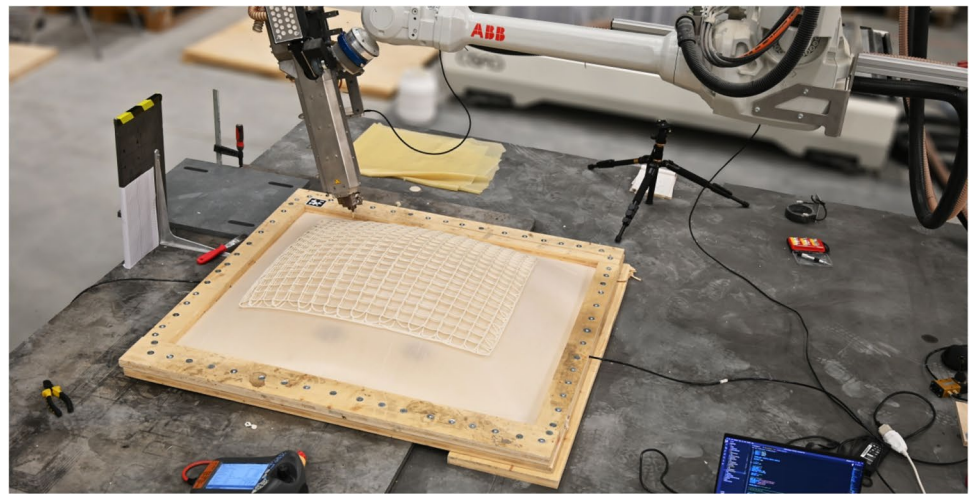
Experiment 3

The aim of Experiment 3 was to improve 3D printing accuracy by investigating the deviation and shape accuracy of the inflatable membrane. Experiment 3 was built within the same fabrication setup and computational process as Experiment 2, except for an optimized scanning process.

Two post-printing scans of the pneumatic formwork have been performed to identify potential deformations caused by the load of the printed object. The scanning step was essential in Experiment 3 to display any deviation from the simulated geometry, see Fig. 12a. After 3D scanning, the reconstructed mesh quad faces were used as a base to generate the fabrication toolpath for Prototype 3. The toolpath was designed with 5 layers of 2 mm height as a more complex geometry for the end-effector to follow the formwork geometry in non-planar coordinates see Fig. 12b. Prototype 3 was 3D printed in PLA and had a slightly higher weight and manufacturing speed of 50 mm/s than Prototype 2, Fig. 12c.

Experiment 3 displayed strategies for improving mesh accuracy in the scanning process for building a more precise and complex geometry. Identifying the pneumatic formwork deviation from the digital simulation was vital for achieving accuracy. The deformation observed by the post-printing scans was heterogeneous. This discrepancy is estimated to be caused by the misaligned mass centers of the printed object and the formwork. Additionally, the increasing weight of the object while 3D printing was not calculated in the pressure control loop, which contributed to further deviation in the inflated membrane. Results showed that the median deviation to the pre-printing scan was 10.42 mm with the printed object and 3.86 mm without the printed object, see Fig. 13. Other factors that can contribute to these deviations are the camera calibration, lighting condition, membrane color, and the point clouds post-processing and surface reconstruction of the mesh. These results confirm the relationship between the 3D-printed object and the formwork deformation.

Fig. 10 **a**) Experiment 2 setup; **b**) Air-pressure loop control system; **c**) Real-time pressure and temperature monitoring. The green line indicates the internal pressure, and the red line indicates the temperature inside the inflatable; **d**) Computational design for Prototype 2; **e**) Prototype 2
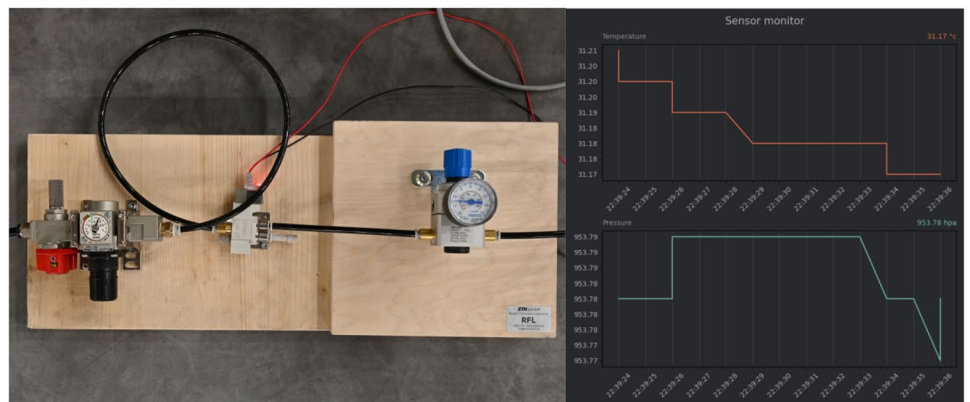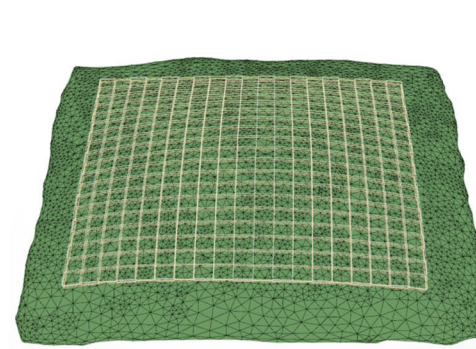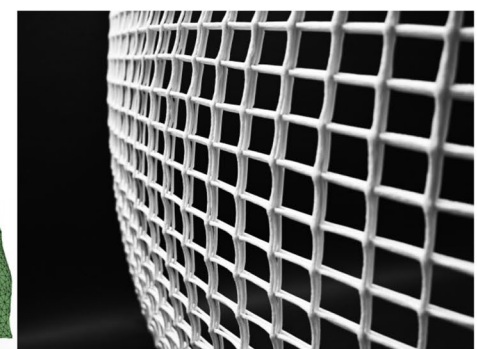

Experiment 4

Experiment 4 aimed to identify the feasibility of 3D printing on a more complex membrane design with a higher-temperature material. Thus, a new boundary was added—a magnet placed in the middle of the formwork to deform the inflated membrane and enable complex freeform designs.

The experiment had the same pneumatic formwork as Experiments 2 and 3. However, the new magnet addition required robot orientations to be integrated to avoid collision during 3D printing. Although, the simulation and

scanning process was similar to Experiment 3. The simulation provided the inflated membrane's geometry and the residual forces of the magnet. The toolpath design for Prototype 4 is a one-layered geometry with a non-planar orientation projected on the scanned mesh, see Fig. 14a. Prototype 4 aimed to display the potential of a more complex geometry design. In the fabrication process of the prototype, a Flir E4 infrared camera monitored the temperature behavior of the extruded material and the membrane, see Fig. 14b [70]. The 0.5 mm silicon membrane was tested
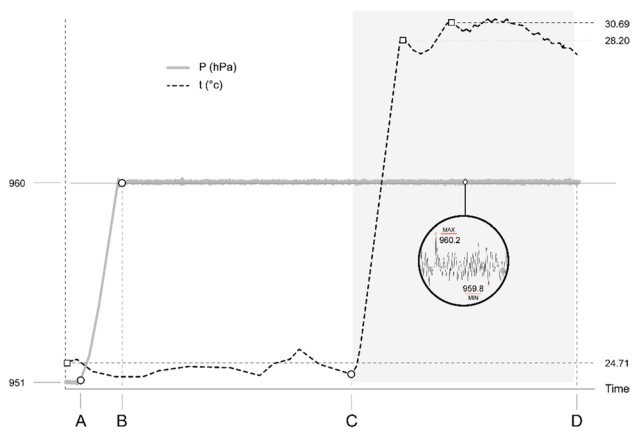
Fig. 11 Performance of the pressure control loop. The gray line indicates the internal pressure during the inflating process and the performance of maintaining target pressure from 951 hPa (A) to 960 hPa (B). The dashed line indicates the temperature difference during the printing process. The temperature of the formwork increases under the influence of the extruded thermoplastic, from 24.71 °C (C) to 30.69 °C

for thermal performance to identify its compatibility with PETG as 3D printing thermoplastic material.

Experiment 4 displayed that a more complex geometry can be designed and manufactured both for the 3D-printed object and the pneumatic formwork. The Prototype 4 fabrication results proved that the membrane could withstand higher thermoplastic melting temperatures of 245 °C compared to its service temperature of 210 °C. The 0.5 mm silicone membrane was undamaged after multiple prints of a total duration of 40 h. It has been observed that, although the extruder has a peak temperature of 245 °C for PETG, the thermal camera recorded a rapid descent to 190~210 °C after extrusion. In addition, the temperature of the thermoplastic drops down further to 70~80 °C within 5 min. Therefore, the silicone membrane could withstand higher temperatures, such as PETG, at 245 °C.

Fig. 12 **a**) Surface reconstruction of the membrane into a mesh and vertices; **b**) Computational design for Prototype 3; **c**) Prototype 3

Fig. 13 Deviation comparison between the formwork without printed object and the simulation result (A). Deviation between the formwork with the printed object and the simulation result (B)

Fig. 14 **a**) Computational design and 3D printed result for Prototype 4; **b**) Thermal imaging of the printing process to determine the compatibility between the silicon membrane and the 3D printing thermoplastic material
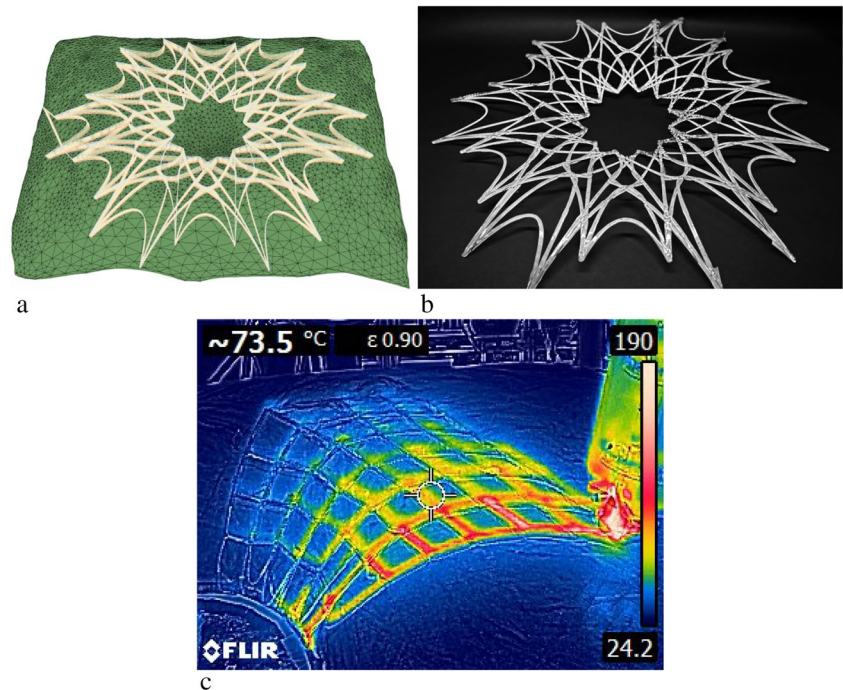

Experiment 5

The final experiment investigated the feasibility of scaling up the prototype's size in a more complex non-planar design.

Pneumatic formwork

For Experiment 5, a pneumatic formwork of 4000×2000 mm was built. The design layering of this pneumatic formwork is similar to Experiments 2, 3, and 4. However, a thicker membrane was selected for Experiment 5, from 35 shore-A1 mm thick silicone. Additionally, a PVC film was applied on the wooden baseboard to reduce air permeability between the membrane and the plywood, see Fig. 15a. Two constraints were added to the membrane to build a more complex inflated geometry. A series of cylindrical super-magnets were evenly distributed on additional wooden board plates. These magnets were used to connect with the metal plates

Fig. 15 **a**) Frame of 4000×2000 mm with metal plates, gasket and film protection; **b**) Magnet constraints placed on the membrane with the additional metallic cylinders; **c**) Original (A) versus optimized TCP frames (B) in the regions close to the extra physical constraints. Colors indicate the angle of TCP normal with respect to the Z direction (UP), from 0 degrees (Blue) to 59 degrees (Red). After TCP adjustment, the maximum relative angle decreased to 29 degrees
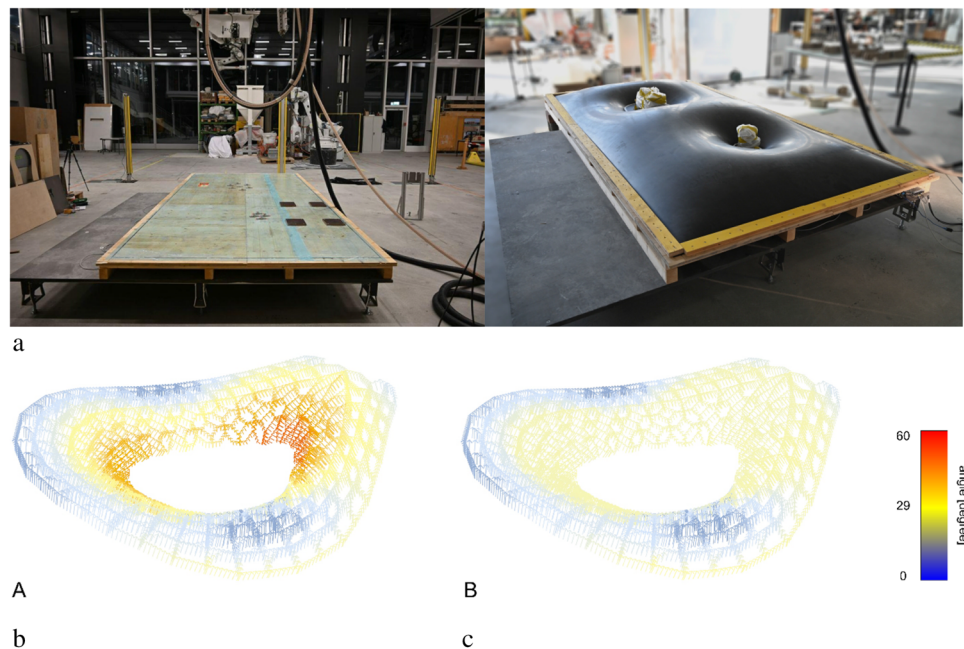
underneath the membrane. As a safety measure, additional metallic cylinders of 20 kg and 40 kg were added on the wooden boards under the magnets to compensate for any redundancies, see Fig. 15b. However, these metallic cylinders increased the collision risk with the extruder. For this reason, an adjustment of the TCP normal was implemented to emphasize the importance of collision avoidance, see Fig. 15c.

Digital design

The computational design of Prototype 5 was generated in four steps, see Fig. 16a. First, two closed polylines representing the internal constraints and the boundary conditions

were used to generate a 2D quad mesh. Second, the mesh was subdivided with the Catmull-Clark algorithm. Third, the 2D quad mesh was projected on the geometry resulting from the dynamic relaxation simulations. Finally, the toolpath was mapped to the scanned result of the pneumatic formwork to generate the 3D print robot trajectories. A pattern gradient ranges from none to single or double side of the pattern for every quad-mesh face, see Fig. 16b. For the toolpath, the layer height varies from 0.5 mm to 2 mm, reflecting the distance from the magnet toward the outer boundary constraints. The toolpath has a lower layer height closer to the magnets to reduce self-weight and 3D printing overhang angle. Therefore, the thickness of the printed parts is optimized and varies from 15 to 60 mm, for 30 printed layers,
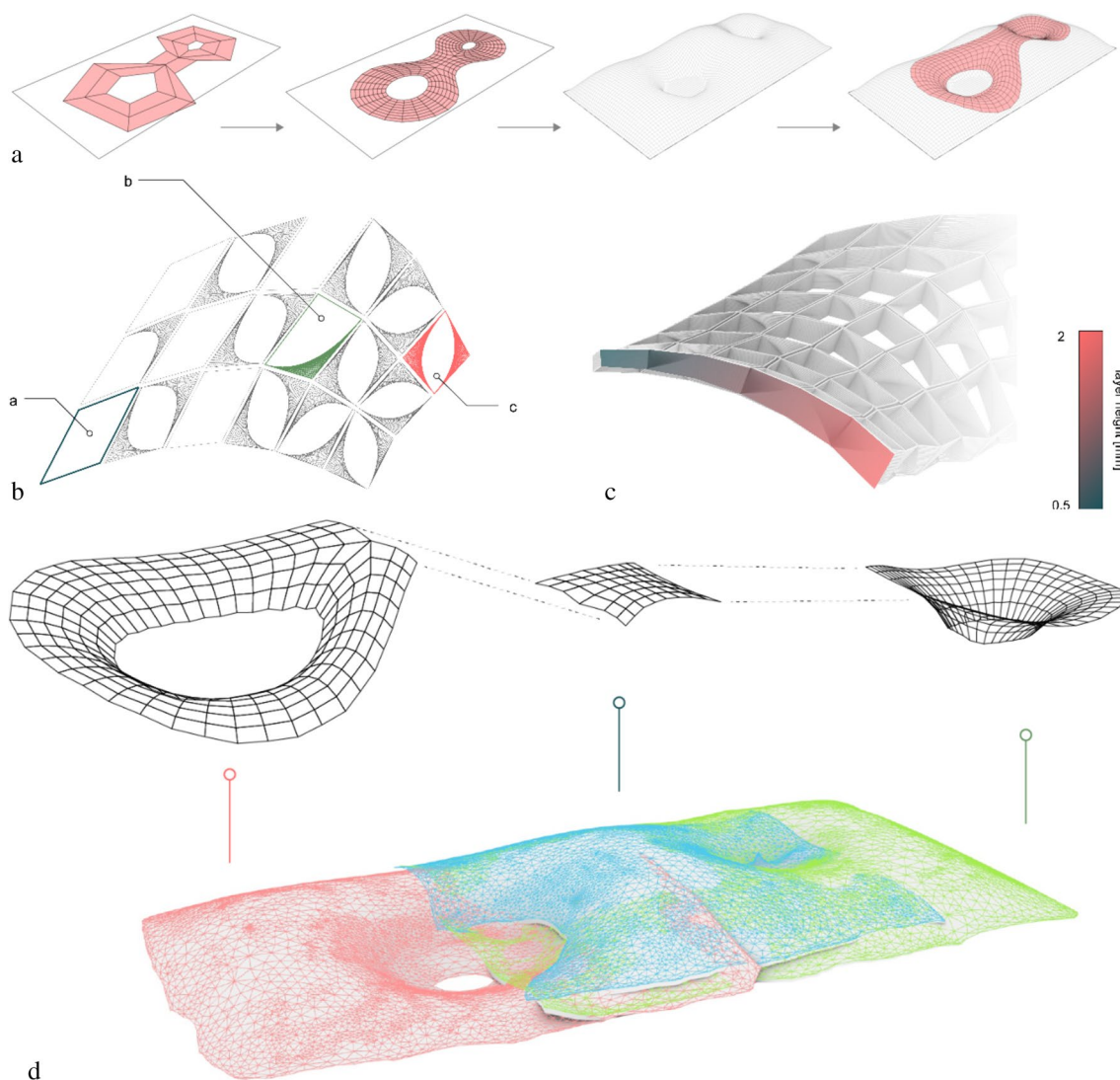

Fig. 16 a) Iterative design for Experiment 5, from boundary condition, to Catmull-Clark subdivision, projected mesh, and toolpath generation; **b**) Patterns within different faces of the mesh, none (a), single-sided (b), and double-sided (c); **c**) Layer height distribution from near to far end with respect to the physical constraints, overlay on section view from 0.5 mm to 2 mm layer height; d) Discretization of the scanning and printing process in three parts

Fig. 16c. Additionally, Prototype 5 design was discretized in three ready-for-fabrication parts to evaluate the scanning process and formwork accuracy in the fabrication process, see Fig. 16d.

Fabrication

Experiment 5 displayed the 3D printing potential of free-form complex geometries on a customizable pneumatic formwork. The prototype was manufactured from PETG pellets with perimeter dimensions of 3200 mm × 1700 mm, see Fig. 17a. Findings from this experiment highlights the importance of the residual forces accuracy in the simulation process, 3D scanning, and air-pressure control loop for the process's repeatability. The repeatability of this new fabrication method is essential for manufacturing multiple samples by reshaping the same pneumatic formwork.

To understand the accuracy and fabrication tolerances of the printing process, it is generally required to compare the fabricated object and the design model. In this study, the nodes were marked with a blue label and the layer width dimensions were used as the comparing parameter (Fig. 17c.) Therefore, the print widths of the first layer were measured in all three parts of the prototype at a total of 186 control points (Fig. 17b). Diagram Fig. 17c displays a difference in deviation distribution of higher values and less accuracy in the outer border of the printed parts. Thus, the areas closer to the magnets have a higher accuracy of the print path design. According to these measurements, an average deviation of 1.57 mm was found.

Experiment 5 proves a successful iterative approach from simulation to scanning, computational design, and fabrication, see Fig. 18. The main findings of this experiment are that additional weights were required to secure the membrane shape compared to the estimated residual forces of 1065 N calculated in the simulation. Six magnets with an adhesive force of 1370 N were used to secure the total simulated residual forces under 5 hPa pressure difference. However, after the target pressure was reached in the membrane, the magnets failed to remain in position. This failure is estimated to be caused by higher values required in the built prototype compared to the simulated distribution of the residual forces. Other finding is regarding the silicon membrane, which decreased to room temperature after approximately 5 layers (10 cm) have been reached. Therefore, several fabrication tests could be manufactured on the same

Fig. 17 **a**) Set-up for large-scale fabrication of the 3D printed prototype on the inflated membrane; **b**) Sample images of Prototype 5 parts (from Left to Right: Part 1, Part 2, and Part 3) with attached blue point labels for the measurements; **c**) Layer width measurements; **d**) Column histogram representing the deviation distribution for three parts of the print. X-axis represents the range of deviation, and Y-axis represent the total amount of measurement fall into corresponding range
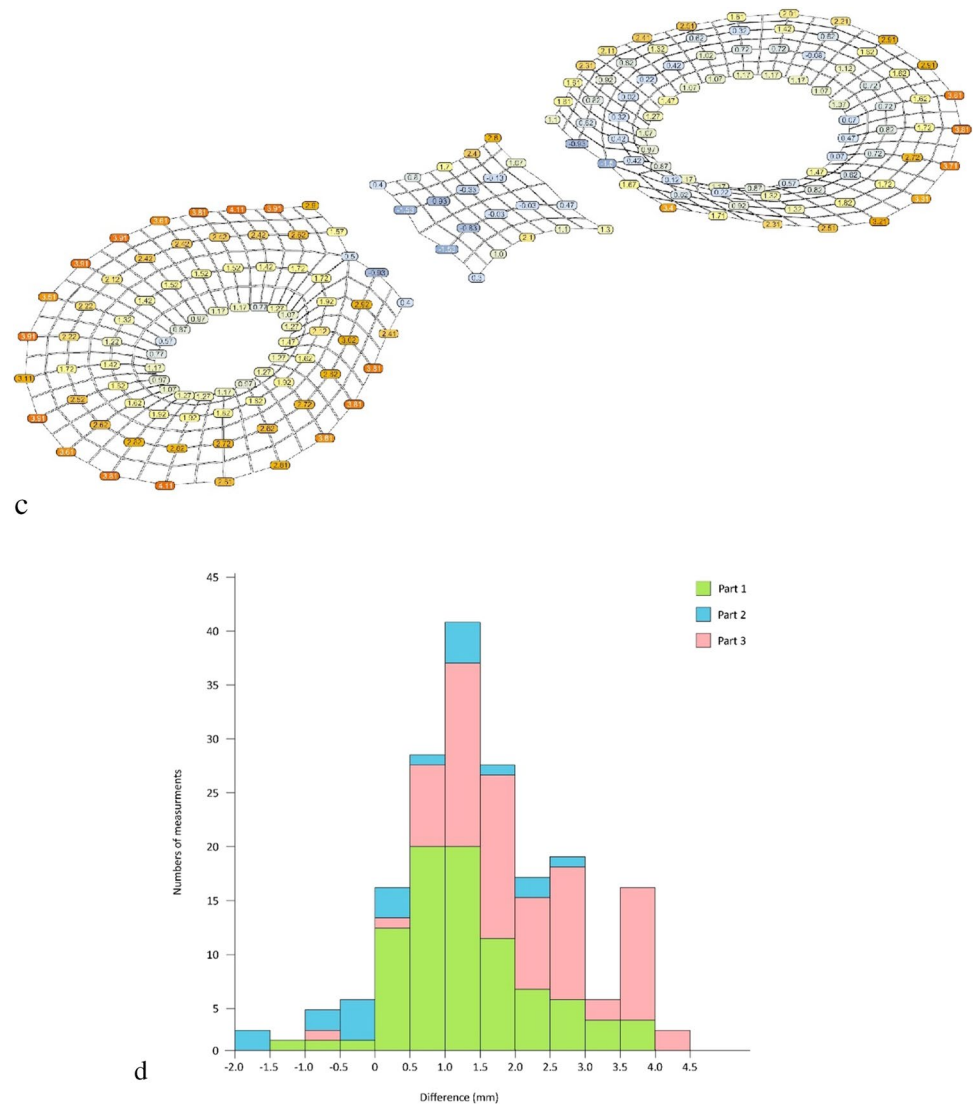

a

b

Fig. 17 (continued)

c

d

Discussion and future work
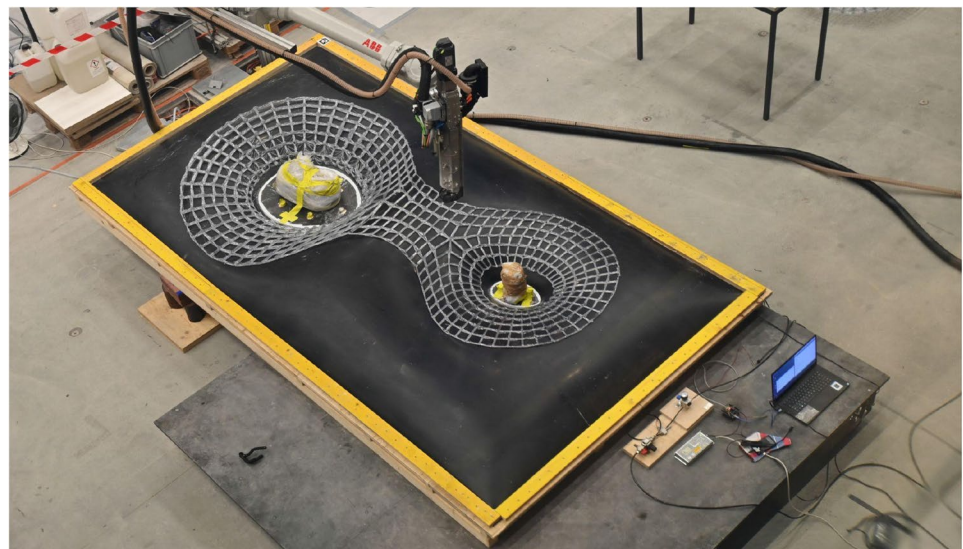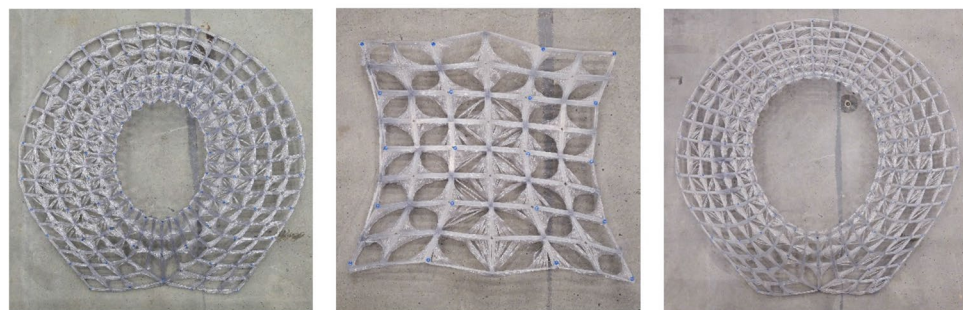
membrane without damaging it. The 3D-printed geometries were similar, proving this experiment's repeatability. This further proved the success of point cloud recorded between multiple scanning sessions.

Discussion and future work

This research investigated the feasibility of robotic 3D printing on a pneumatic formwork, named PneuPrint. The experimental work displayed several findings regarding challenges towards large-scale fabrication. First, the 3D scanning and simulation are essential for designing the pneumatic formwork. The material properties, pneumatic pressure, and boundary conditions are the main parameters to consider for shaping the physical prototype. Nonetheless, the membrane can deform due to imperfections and environmental disturbance. For this reason, the scanning process can help identify if the physical prototype is similar to the digital model. Additionally, the 3D scanning process helps to prevent collision between the extruder nozzle and the inflated formwork. Environmental noise reduction and surface reconstruction were used in this study to improve the scanning precision. Only then, the computational design and toolpath generation were generated. Another challenge of this process is the deformation of the pneumatic formwork during the 3D printing process because of the additional 3D print weight. These membrane deformations create surface deviation from the printed object to the toolpath, which later lead to inaccuracies in the 3D printed prototype.

Nevertheless, the proposed PneuPrint technique illustrates several advantages regarding complex non-planar 3D printing. It does not rely on additional auxiliary scaffolding and supports, which enables cost-effective and low-greenhouse emissions formwork for building envelopes. With this technique, the design of the 3D-printed object can be integrated or independent from the inflated geometry.
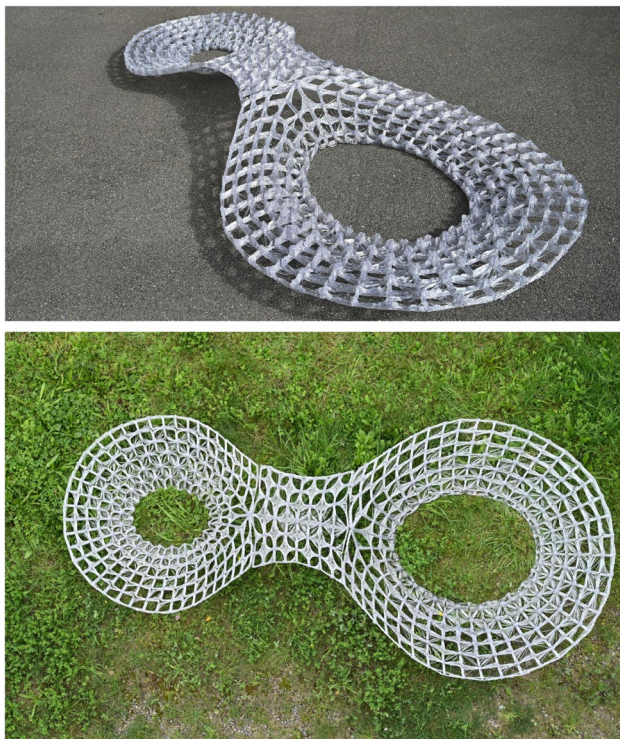
Fig. 18 Experiment 5 perspective view (top picture) and bird-eye view (below picture)

Compared with conventional 3D printing, the PneuPrint technique can significantly improve the printing quality regarding overhangs and the smoothness of the surface where printed supports are required. Additionally, the 3D-printed design can have a much wider shape variety because the pneumatic formwork enables further non-planar fabrication opportunities. Experiment 5, specifically displays the manufacturing potential of non-planar designs for large-scale prototypes. Such complex shapes have a high potential to be used for building envelope designs, such as facade elements, or interior wall dividers. The architectural application of these elements can consider integrating or removing the pneumatic formwork in the post-fabrication process.

Future work can explore non-planar designs with different constraints beyond the magnets used in our experiments. A good control on the membrane pressure is essential for large-scale 3D printings supports. Further tests can investigate how to improve print accuracy and determine the correlation between the weight of the 3D printed part and the membrane support. Additionally, the scanning accuracy can be improved if markers are applied on the membrane to calibrate the scanning location. Sensors can also be integrated into the robotic fabrication system, enabling constant real-time feedback between the actual printing interface and the digital generation of the printing location. Furthermore, the authors recommend exploring other 3D printing materials for this novel large-scale process.

Declarations

References

1. Wong JF (2010) The text of free-form architecture: qualitative study of the discourse of four architects. Des Stud 31(3):237–267
2. Pottmann H (2008) Geometry of architectural freeform structures. Proc 2008 ACM Symp Solid Phys Model 2008, SPM'08 209(209):9
3. Kim K, Son K, Kim ED, Kim S (2015) Current trends and future directions of free-form building technology. Archit Sci Rev 58(3):230–243
4. Colbert F (2003) The Sydney Opera House : An Australian Icon. Int J Arts Manag 5(2):69–77
5. Sü-gül Z, Çalışkan M (2010) Acoustical considerations in the design of Heydar Aliyev Center auditorium. In: Proceedings of the international symposium on room acoustics, ISRA 2010. pp 1–7
6. Penttilä H (2006) Describing the changes in architectural information technology to understand design complexity and freeform architectural expression. Electron J Inf Technol Constr 11(February):395–408
7. Henriksson V, Hult M (2015) Rationalizing freeform architecture. [Master Thesis, Chalmers University of Technology]

8. Rippmann M (2016) Funicular shell design: geometric approaches to form finding and fabrication of discrete funicular structures. [Doctoral thesis, ETH Zürich]

9. Pottmann H, Wallner J (2017) Freeform architecture and discrete differential geometry. In: discrete geometry for computer imagery: 20th IAPR international conference, DGCI 2017, Vienna, Austria, September 19–21, 2017, Proceedings. 20, pp 3–8

10. Castañeda E, Lauret B, Lirola JM, Ovando G (2015) Free-form architectural envelopes: Digital processes opportunities of industrial production at a reasonable price. J Facade Des Eng 3(1):1–13

11. Haghir S, Haghnazar R, SaghafiMoghaddam S, Keramat D, Matini MR, Taghizade K (2021) BIM based decision-support tool for automating design to fabrication process of freeform lattice space structure. Int J Sp Struct 36(3):164–179

12. Majowiecki M (2008) Ethics and Structural Reliability in Free-Form Design (FFD). J Int Assoc Shell Spat Struct 48(156):29–50

13. Mitchell WJ (1998) Articulate design of free-form structures. In: Artificial intelligence in structural engineering. Lecture Notes in Computer Science, vol 1454, pp 223–234

14. Eigensatz M, Kilian M, Schiftner A, Mitra NJ, Pottmann H, Pauly M (2010) Paneling architectural freeform surfaces. In: SIGGRAPH '10: special interest group on computer graphics and interactive techniques. Los Angeles, California, vol 1, no 212, p 1

15. Beaman JJ, Barlow JW, Bourell DL, Crawford RH, Marcus HL, McAlea KP (1997) Solid freeform fabrication: a new direction in manufacturing, vol 2061. Kluwer Academic Publishers, Norwell, MA

16. Bañón C, Raspall F (2021) 3D pectural design and construction: a systematic literature reviewnds. Springer, Berlin/Heidelberg, Germany

17. Žujović M, Obradović R, Rakonjac I, Milošević J (2022) 3D printing technologies in architectural design and construction: a systematic literature review. Buildings 12(9):1319

18. Berman B (2012) 3-D printing: The new industrial revolution. Bus Horiz 55(2):155–162

19. Wu P, Wang J, Wang X (2016) A critical review of the use of 3-D printing in the construction industry. Autom Constr 68:21–31

20. Sakin M, Kiroglu YC (2017) 3D printing of buildings: Construction of the sustainable houses of the future by BIM. Energy Procedia 134:702–711

21 Tay YWD, Panda B, Paul SC, Noor Mohamed NA, Tan MJ, Leong KF (2017) 3D printing trends in building and construction industry: a review. Virtual Phys Prototyp 12(3):261–276

22. Additive manufacturing - material extrusion-based additive manufacturing of plastic materials - part 1: feedstock materials. ISO/ASTM 52903-1:2020(en). Technical Committee : ISO/TC 261 Additive manufacturing, 2020. [Online]. Available: https://www.iso.org/standard/67290.html. Accessed 09 Mar 2023

23. Ghasemieshkaftaki M, Ortiz MA, Bluyssen PM (2021) An overview of transparent and translucent 3D-printed façade prototypes and technologies. In: Proceedings of the healthy buildings Europe 2021 Online Conference. Oslo, Norway, pp 21–23

24. Wangler T, Roussel N, Bos FP, Salet TAM, Flatt RJ (2019) Digital concrete: a review. Cem Concr Res 123:105780

25. Wangler T et al (2016) Digital concrete: opportunities and challenges. RILEM Tech Lett 1:67–75

26. Wolf A, Rosendahl PL, Knaack U (2022) Additive manufacturing of clay and ceramic building components. Autom Constr 133(May 2021):103956

27. Gardner L, Kyvelou P, Herbert G, Buchanan C (2020) Testing and initial verification of the world's first metal 3D printed bridge. J Constr Steel Res 172:106233

28. Evans SI, Wang J, Qin J, He Y, Shepherd P, Ding J (2022) A review of WAAM for steel construction – Manufacturing, material and geometric properties, design, and future directions. Structures 44(August):1506–1522

29 Buchanan C, Gardner L (2019) Metal 3D printing in construction: A review of methods, research, applications, opportunities and challenges. Eng Struct 180(March 2018):332–348

30. Mitropoulou I, Bernhard M, Dillenburger B (2020) Print paths key-framing: design for non-planar layered robotic FDM printing. In: Proceedings of the 5th annual ACM symposium on computational fabrication. pp 1–10

31. Cendrero AM, Fortunato GM, Munoz-Guijosa JM, De Maria C, Lantada AD (2021) Benefits of non-planar printing strategies towards eco-efficient 3d printing. Sustain 13(4):1–17

32. Krčma M, Paloušek D (2022) Comparison of the effects of multiaxis printing strategies on large - scale 3D printed surface quality, accuracy, and strength. Int J Adv Manuf Technol 119(11-12):7109–7120

33 Evans B (2012) Practical 3D printers: The science and art of 3D printing. Apress

34. Schmidt R, Umetani N (2014) Branching support structures for 3D printing. In: SIGGRAPH '14 proceedings: special interest group on computer graphics and ineractive techniques conference. Vancouver, Canada, vol 9, p 1

35. Zhang X, Wang CCL (2015) Perceptual models of preference in 3D printing direction. ACM transactions on graphics (TOG) 34(6) 215:1–12

36. Barnett E, Gosselin C (2015) Large-scale 3D printing with a cable-suspended robot. Addit Manuf 7:27–44

37. Hajash K, Sparrman B, Guberan C, Laucks J, Tibbits S (2017) Large-scale rapid liquid printing. 3D Print Addit Manuf 4(3):123–132

38. NorthSails (n.d.) 3Di Technology. https://www.northsails.com/. Accesed on 20.03.2023

39. Raun C, Kirkegaard PH (2014) Adaptive mould-A cost-effective mould system linking design and manufacturing of double-curved GFRC panels. In: Proceedings of IASS annual symposia. vol 2014, no 11, pp 1–7

40. Battaglia CA, Miller MF, Zivkovic S (2019) Sub-Additive 3D printing of optimized double curved concrete lattice structures. Robot Fabr Archit Art Des 2018:242–255

41 Li W, Lin X, Bao DW, Min Xie Y (2022) A review of formwork systems for modern concrete construction. Structures 38(July 2021):52–63

42. Chudley R, Greeno R (2006) Advanced construction technology. Pearson Education, Harlow

43. Hawkins WJ et al (2016) Flexible formwork technologies – a state of the art review. Struct Concr 17(6):911–935

44. Chuang C, Chilton J (2016) Design and modelling of Heinz Isler's Sicli shell. In: Proceedings of IASS annual symposia. vol 2016, no 2, pp 1–10

45 West M (2016) The fabric formwork book: Methods for building new architectural and structural forms in concrete. Routledge

46. Spahiu T, Grimmelsmann N, Ehrmann A (2017) Effect of 3D printing on textile fabric. In: 1st international conference "engineering and entrepreneurship" proceedings. no (1), pp 1–7

47. Malengier B, Hertleer C, Van Langenhove L, Cardon L (2017) 3D printing on textiles: testing of adhesion. In: International conference on intelligent textiles and mass customisation. vol 1, pp 1–6

48. Kladeftira M et al (2022) Digital bamboo: a study on bamboo, 3D printed joints, and digitally fabricated building components for ultralight architectures. In: Acadia 2022: Hybrids & Haecceities

49. Coulter FB, Coulter BS, Papastavrou E, Ianakiev A (2018) Production techniques for 3D printed inflatable elastomer structures: Part II-Four-axis direct ink writing on irregular double-curved and inflatable surfaces. 3D Print Addit Manuf 5(1):17–27

50. Dörstelmann M et al (2015) ICD/ITKE research pavilion 2014–15: Fibre placement on a pneumatic body based on a water spider web. Archit Des 85(5):60–65

51. Van Mele T, De Laet L, Veenendaal D, Mollaert M, Block P (2013) Shaping tension structures with actively bent linear elements. Int J Sp Struct 28(3–4):127–135

52. Datenblatt (n.d.) SCS Silikon Membrane. https://shop.swiss-composite.ch/. Accesed on 03.08.2022

53. Steinbach AG (2015) Technisches Datenblatt silicone 35 black. Forming & conveying solutions, [online]. Available: https://www.

steinbach-ag.de/de/forming-solutions/produkte/produktgruppe/silicone-35-black.html. Accessed 24 May 2023

54. Brandner R (2013) Production and technology of cross laminated timber (CLT): a state-of-the-art report. In: Focus solid timber solutions-European conference on cross laminated timber (CLT). University of Bath, Bath, UK, vol 21, pp. 3–36

55. COMPAS: A framework for computational research in architecture and structures. https://compas.dev/. Accesed on 20.03.2023

56. plugin for Rhinoceros (n.d.) Visual programming language. https://www.rhino3d.com/6/new/grasshopper. Accesed on 04.06.2020

57. Depth Camera D415. Intel® RealSense™ depth and tracking cameras. [Online]. Available: https://www.intelrealsense.com/depth-camera-d415/. Accessed 13 Dec 2022

58. AprilTag (n.d.) AprilTags Visual Fiducial System. https://april.eecs.umich.edu/software/apriltag. Accesed on 23.03.2023

59. Open3D (n.d.) A Modern Library for 3D Data Processing. https://arxiv.org/abs/1801.09847. Accesed on 23.03.2023

60. Besl PJ, McKay ND (1992) Method for registration of 3-D shapes. Sens Fusion IV Control Paradig Data Struct 1611(April 1992):586–606

61. Kazhdan M, Bolitho M, Hoppe H (2006) Poisson surface reconstruction. In: Proceedings of the fourth eurographics symposium on geometry processing. vol 7

62. Fleischmann P, Casas G, Lyrenmann M (n.d.) COMPAS RRC: Online control for ABB robots over a simple-to-use Python interface. https://compas-rrc.github.io/compas_rrc/latest/. Accesed on 28.03.2023

63. Connolly C (2009) Technology and applications of ABB RobotStudio. Ind Rob 36(6):540–545

64. UR5 (n.d.) Universal Robots. https://www.universal-robots.com/. Accesed on 02.03.2023

65. E3DOnline (n.d.) SuperVolcano Upgrade Kit. https://e3d-online.com/. Accesed on 05.03.2023

66. Vidakis N, Petousis M, Velidakis E, Liebscher M, Mechtcherine V, Tzounis L (2020) On the strain rate sensitivity of fused filament fabrication (Fff) processed pla, abs, petg, pa6, and pp thermoplastic polymers. Polymers (Basel) 12(12):1–15

67. Robotic_Fabrication_Laboratory (n.d.) © Gramazio Kohler Research, ETH Zurich. https://ita.arch.ethz.ch/archteclab/rfl.html. Accesed on 23.10.2022

68. ABB (n.d.) Industrial Robots. https://new.abb.com/products/robotics/industrial-robots. Accesed on 23.03.2023

69. CEAD_Extruder (n.d.) Pellet extruder for composite thermoplastic 3D printing. https://robotextruder.com/. Accesed on 23.10.2020

70. TeledyneFlir (n.d.) FLIR E4 Infrared Camera with MSX®. https://www.flir.eu/. Accesed on 24.03.2023